Colloids and Surfaces B: Biointerfaces 213 (2022) 112400

Contents lists available at ScienceDirect

Colloids and Surfaces B: Biointerfaces

journal homepage: www.elsevier.com/locate/colsurfb

In silico study of substrate chemistry effect on the tethering of engineered antibodies for SARS-CoV-2 detection: Amorphous silica *vs* gold

Didac Martí [a,b], Eduard Martín-Martínez [a], Juan Torras [a,b,*], Oscar Betran [c], Pau Turon [d,**], Carlos Alemán [a,b,e,*]

[a] Departament d'Enginyeria Química (DEQ), EEBE, Universitat Politècnica de Catalunya (UPC), C/ Eduard Maristany, 10-14, Ed. I2, 08019 Barcelona, Spain
[b] Barcelona Research Center in Multiscale Science and Engineering, Universitat Politècnica de Catalunya, C/ Eduard Maristany, 10-14, 08019 Barcelona, Spain
[c] Departament de Física, EETAC, Universitat Politècnica de Catalunya (UPC), c/ Esteve Terrades, 7, 08860 Castelldefels, Spain
[d] B. Braun Surgical, S.A.U. Carretera de Terrasa 121, Rubí, 08191 Barcelona, Spain
[e] Institute for Bioengineering of Catalonia (IBEC), The Barcelona Institute of Science and Technology, Baldiri Reixac 10-12, 08028 Barcelona, Spain

ARTICLE INFO

Keywords:
Antibody immobilization
Amorphous silica
Gold
Molecular Dynamics
SARS-CoV-2 immunosensor

ABSTRACT

The influence of the properties of different solid substrates on the tethering of two antibodies, IgG1-CR3022 and IgG1-S309, which were specifically engineered for the detection of SARS-CoV-2, has been examined at the molecular level using conventional and accelerated Molecular Dynamics (cMD and aMD, respectively). Two surfaces with very different properties and widely used in immunosensors for diagnosis, amorphous silica and the most stable facet of the face-centered cubic gold structure, have been considered. The effects of such surfaces on the structure and orientation of the immobilized antibodies have been determined by quantifying the tilt and hinge angles that describe the orientation and shape of the antibody, respectively, and the dihedrals that measure the relative position of the antibody arms with respect to the surface. Results show that the interactions with amorphous silica, which are mainly electrostatic due to the charged nature of the surface, help to preserve the orientation and structure of the antibodies, especially of the IgG1-CR3022, indicating that the primary sequence of those antibodies also plays some role. Instead, short-range van der Waals interactions with the inert gold surface cause a higher degree tilting and fraying of the antibodies with respect to amorphous silica. The interactions between the antibodies and the surface also affect the correlation among the different angles and dihedrals, which increases with their strength. Overall, results explain why amorphous silica substrates are frequently used to immobilize antibodies in immunosensors.

1. Introduction

The effect of surface chemistry on the stability and activity of immobilized proteins is critical in many fields, including biosensing, drug delivery and biofuel cells [1–8]. Because of this influence, the immobilization of proteins has been investigated using a variety of support materials, as for example gold [9,10], silica [11,12], carbon nanotubes [13,14], graphene [15,16], and self-assembled monolayers [17,18]. Although the stability of the protein on the support was found to be determined by the effect of intermolecular interactions on intramolecular ones, experimental evaluation of the interactions between the protein and the solid-surface is not an easy task. Thus, determination of the strength of the interactions on the macroscale using adsorption capacity measures and electrical signals is not adequate. Instead, microscale measures using, for example, atomic force microscopy (AFM)-based methods enable quantification of the force between single protein molecules and the substrate surface [2,19–23], even though identification of the key microscopic features affecting the stability of the immobilized protein is not possible.

Molecular simulation approaches have been revealed as powerful tools for reaching detailed understanding of the stability of immobilized biomolecules [24–33]. At present time these techniques are precise enough to evaluate the effect of the surface on the orientation and conformation of the immobilized biomolecules at the molecular and

* Corresponding authors at: Departament d'Enginyeria Química (DEQ), EEBE, Universitat Politècnica de Catalunya (UPC), C/ Eduard Maristany, 10-14, Ed. I2, 08019 Barcelona, Spain.
** Corresponding author.
E-mail addresses: joan.torras@upc.edu (J. Torras), pau.turon@bbraun.com (P. Turon), carlos.aleman@upc.edu (C. Alemán).

https://doi.org/10.1016/j.colsurfb.2022.112400
Received 10 January 2022; Received in revised form 4 February 2022; Accepted 4 February 2022
Available online 7 February 2022

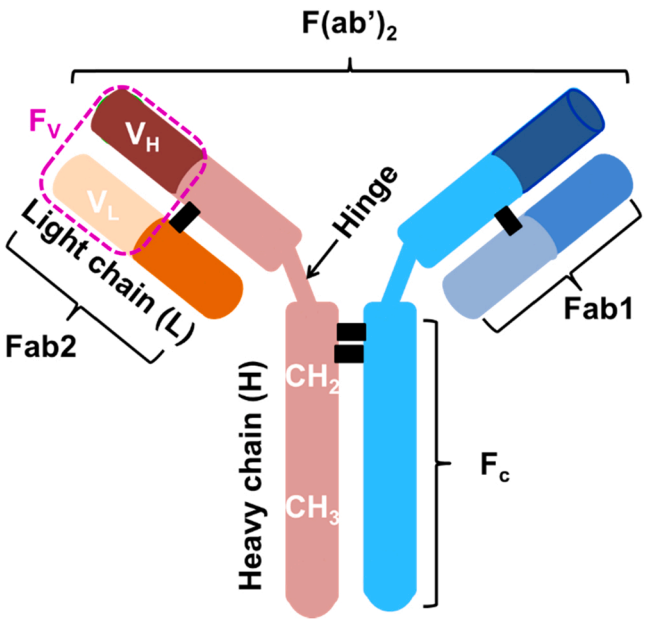

Scheme 1. Parts of the Y-like shape IgG antibodies.

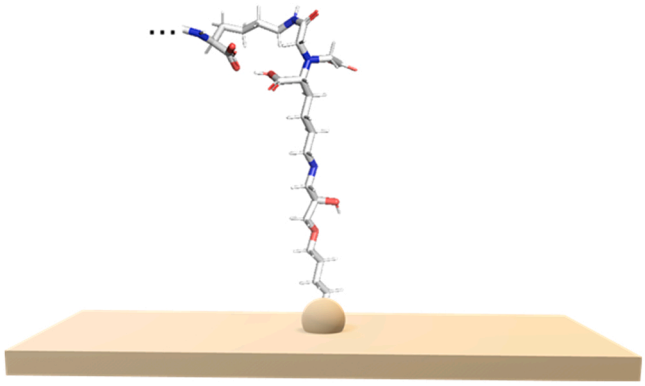

Scheme 2. Linker obtained by modifying the Lys478 residue of IgG1-CR3022 and IgG1-S309, respectively, when immobilized on amorphous silica. The sphere at the bottom part corresponds to a Si atom.

atomistic levels. In that perspective, the role of molecular simulation is becoming increasingly important not only in revealing the mechanism of chemical and biological processes taking place at the interface but also in designing new therapeutic products. In particular, molecular simulation studies based on the combination of different approaches, as for example multi-scale methods that combine all-atom and coarse-grain classical models [32,33] and approaches based on the utilization of different methods to scan the corresponding potential energy surfaces [25,34,35], have been found to be promising tools, providing important achievements within this field.

The emergence in 2019 of SARS-CoV-2 has had devastating consequences on public health, economy and society. In addition to the urgency of vaccines (*i.e.* biological treatment) needed to reduce the morbidity and mortality associated with COVID-19 pandemic [36,37], the inactivation of SARS-CoV-2 using different strategies based on chemical and physical treatments became a major objective. Thus, chemical agents were used to disinfect inanimate surfaces [38,39] and deactivate the virus in culture media [40], whereas thermal inactivation [41,42], cold plasma [43] and far-UVC light [44] were physical treatments employed to eliminate the virus in surfaces, air and water.

Once the inactivation of the virus has been dealt with relative success, development of rapid and efficient immunosensors for early detection in the diagnosis of SARS-CoV-2 is becoming a topic of increasing interest [45–48]. In general, immunosensors for the detection of SARS-CoV-2 are based on the development of specific neutralizing antibodies able to bind the target for identification (*e.g.* viral RNA and proteins), and the amplification of signals and transduction systems (*e.g.* electrical, surface plasmon resonance, electrochemical, optical, mechanical systems, and fluorescent). The recognition between the antibody and the target can be identified through the conformational alterations. Within this context, we recently engineered two immunoglobulin G (IgG)-like antibodies to specifically detect SARS-CoV-2 [25]. This was achieved combining the crystal structure of the fragment antigen binding (Fab) of the CR3022 [49] or the variable domains (Fv) of the S309 [50] (Scheme 1), which are neutralizing antibodies that tightly bound to SARS-CoV-2 receptor-binding domain (RBD), with the crystal structure of IgG1 B12 antibody [51], which was used to inactivate the human immunodeficiency virus-1 (HIV-1). The Fab of CR3022 is formed by the association of the light chains with the variable domain of the heavy chain (V_H) and the first constant domain (CH_1), whereas the Fv of S309 involves the variable domains of the heavy and light chains (V_H and V_L, respectively).

SARS-CoV-2 RBD plays a key role in the infection process, binding the angiotensin converting enzyme 2 (ACE2) to form an RBD/ACE2 complex, which culminates with the fusion of the target cell membrane [52,53]. Accordingly, the choice of CR3022 and S309 neutralizing antibodies was based on the fact that they do not compete with the ACE2 binding site when binds SARS-CoV-2 [54,55]. Of the two engineered antibodies, named IgG1-S309 and IgG1-CR3022, the former was found to be the most stable from a structural point of view when tethered on a chemically inert surface (*i.e.* gold), preserving the conformation of the Fab of neutralizing S309 antibody [25].

In this work we examine the effect of a solid substrate with a rich surface chemistry on the orientation of IgG1-S309 and IgG1-CR3022 using detailed computer simulation methods. For this purpose, the two engineered antibodies have been immobilized on amorphous silica, which consists of a network of silicon and oxygen (SiO_2) with an outermost hydroxylated layer (*i.e.* covered at the surface by the so-called silanol groups, Si–OH). In order to illustrate the influence of the surface chemistry on the structure of the tethered antibodies and, therefore, on the immunosensing process, results obtained for amorphous silica have been systematically compared with those reported for gold [25]. Thus, the surface properties of amorphous silica (*e.g.* polarity, hydrogen bonding capacity and hydrophilicity), which are conferred by the surface hydroxylation [56], are completely different from those of gold, which is a crystalline solid that organizes in a face centered cubic (FCC) cell and displays a chemically inert surface. Despite of such significant differences, it should be remarked that both amorphous silica and gold are frequently used as substrates for virus immunosensors [57–61]. All-atom classical molecular dynamics (MD) simulations of IgG1-CR3022 and IgG1-S309 tethered on amorphous silica and gold substrates have been conducted using two different methodologies: conventional MD (cMD) and accelerated MD (aMD). Results reflect that long-range electrostatic interactions between the surface and the antibody arms play a major role in the orientation and stability of the immobilized protein and, therefore, in the activity retention. Thus, the orientation of the two studied antibodies was more appropriated for immunosensing when the substrate was amorphous silica than gold.

2. Methods

2.1. Construction of the amorphous silica and gold surfaces

The outermost layer of amorphous silica was constructed by applying a rigorous annealing process to an α-cristobalite slab of $50 \times 50 \times 15$ Å^3. For this purpose, three heating-cooling cycles were applied, as is described in the Electronic Supporting Information. The annealing process was conducted using a cMD approach, as

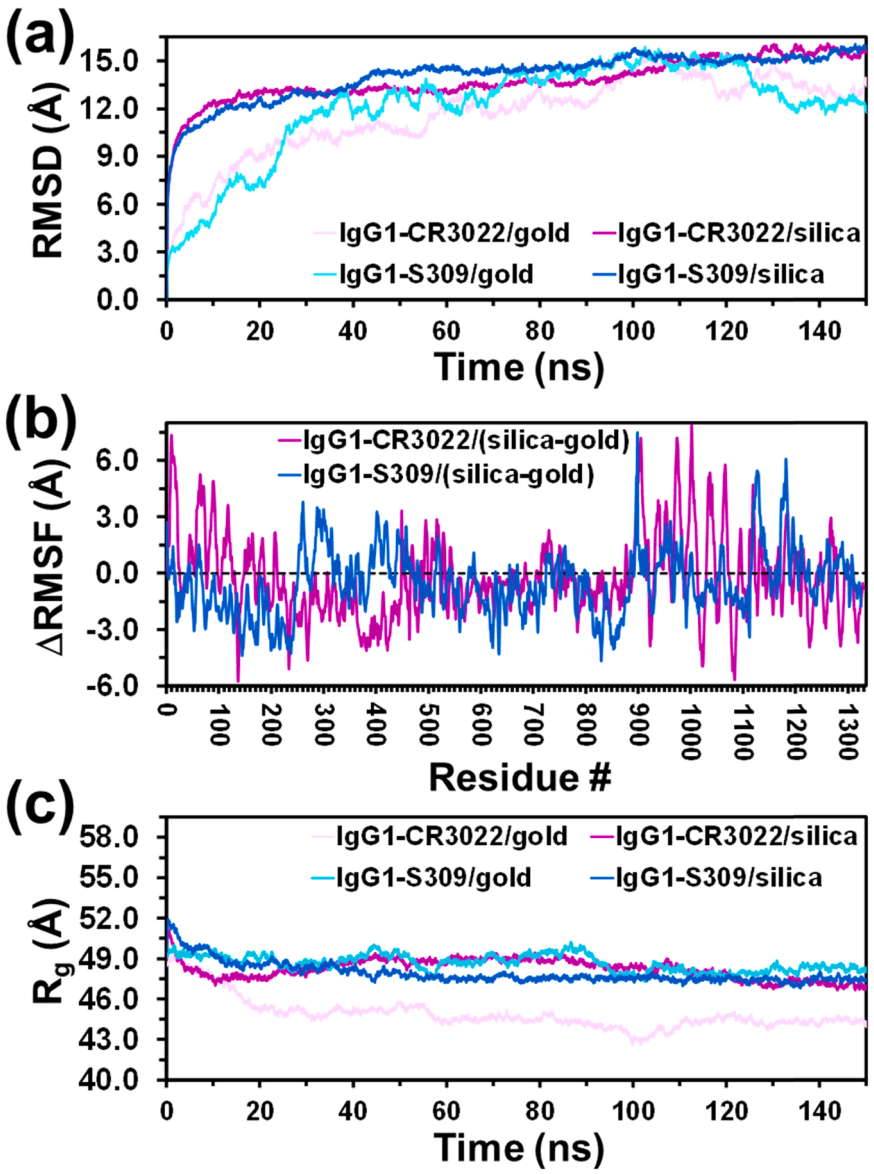

Fig. 1. (a) RMSD, (b) ΔRMSF and (c) R_g for the engineered antibodies. (a) and (c) display the temporal evolution of the RMSD and R_g for IgG1-CR3022 and IgG1-S309 immobilized on silica and gold, whereas (b) shows the difference between the RMSF values obtained for the antibody immobilized on silica and gold.

Table 1
Average[a] RMSD, RMSF and R_g values for IgG1-CR3022 and IgG1-S309 immobilized on silica and gold.

	IgG1-CR3022		IgG1-S309	
	Silica	Gold	Silica	Gold
RMSD (Å)	13.5 ± 0.9	13.9 ± 1.1	14.8 ± 0.8	15.1 ± 0.3
RMSF (Å)	4.8 ± 2.1	5.1 ± 1.4	4.6 ± 1.6	5.2 ± 1.3
R_g (Å)	48.0 ± 0.7	44.2 ± 0.4	47.5 ± 0.2	48.4 ± 0.6

[a] Averaged over the last 70 ns of simulation.

implemented in the DLPOLY 4 program [62], and applying the Tersoff potential for bulk silica [63]. After the final annealing process, the slab was replicated in the *x*- and *y*-axis in order to obtain a larger slab of $180 \times 180 \times 20$ Å^3 and relaxed using cMD. Finally, the large surface was hydrolyzed by randomly adding hydrogen atoms to the unsaturated surface oxygen atoms, at the equilibrium distance, until a final density of 1.68 hydrogen atoms per nm^2 was reached. The physical properties of amorphous silica constructed using this strategy match experimental values, as was previously demonstrated [25,64].

Simulations of the antibodies immobilized on gold were performed considering a nine-layered slab with dimensions 179.5×180.3 Å^2, representing the (111) facet of the FCC unit cell [25]. The crystallographic parameter for gold was defined as $a = 2.89$ Å.

2.2. Immobilization of IgG1-CR3022 and IgG1-S309 antibodies

The engineering approach followed to construct IgG1-CR3022 and IgG1-S309 antibodies was reported in a previous work [25], where a complete description of the procedure can be found. The IgG1-CR3022 and IgG1-S309 antibodies contained a total of 1331 and 1327 residues, respectively. Figs. S1 and S2 list the sequence of each antibody, specifying the origin of the different tracts.

Engineered antibodies were linked to the studied surfaces through a Lys residue located at the fragment crystalline (Fc) region (*i.e.* Lys478 for both IgG1-CR3022 and IgG1-S309, respectively), which led to an almost perfect perpendicular alignment as starting point. As the density of chemisorbed antibodies in immunosensors is low, we have omitted the effect of neighboring antibody molecules and focused only on the

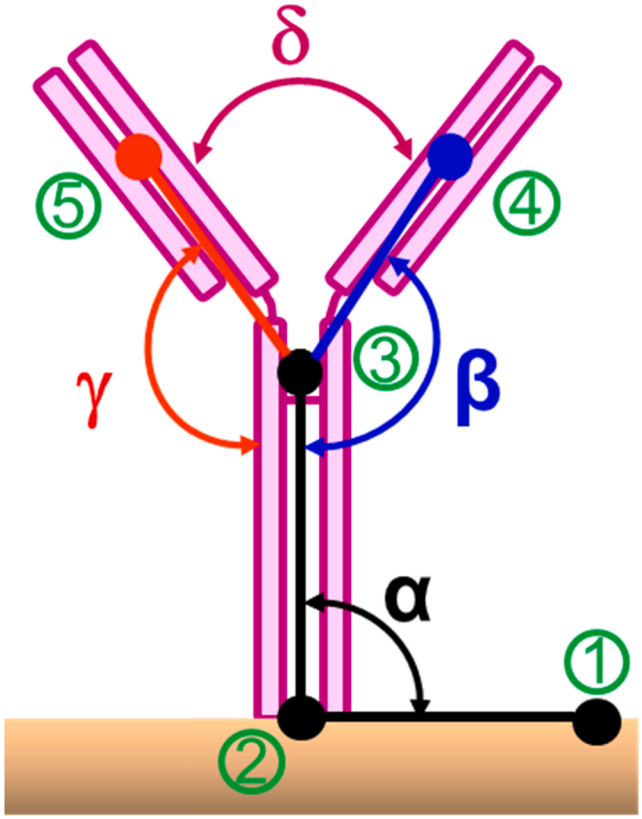

Scheme 3. Sketch displaying the α (1–2–3), β (2–3–4), γ (2–3–5) and δ (4–3–5) angles. The meaning of 1, 2, 3 and 4 is described in the text.

effect of the surface. The approach used to immobilize the engineered antibodies on the amorphous silica and gold surfaces was based on the activation of the surface with carboxylic groups that reacted with the terminal amino side group of the above mentioned Lys residue. Scheme 2 sketches the covalent linker used to immobilize the antibodies on silica. The resulting modified residue (*i.e.* the linker) was built for the simulations. Besides, the covalent linker used for the simulations on the gold surface were reported in previous work [25].

2.3. Solvation, charge neutralization and force-field

Charge neutralization was performed with the addition of 4 and 5 Na^+ counterions for IgG1-CR3022 and the IgG1-S309, respectively, which were initially located in the neighborhood of negatively charged residues, respectively. Afterwards, antibody-functionalized surfaces were solvated with 162597 explicit water molecules.

Classical simulations were performed using the AMBER 18 simulation package [65]. The AmberTools Leap program was used to set up input files for MD simulations with Amber. The Amber ff03ua force field [66] was used for all the protein atoms except to those belonging to the linker, the Lennard-Jones parameters developed by Huff et al. [67] and by Heinz et al. [68] for the amorphous silica and face centered cubic

Table 2
Average[a] α, β and γ RMSF and R_g values for IgG1-CR3022 and IgG1-S309 immobilized on silica and gold.

	IgG1-CR3022		IgG1-S309	
	Silica	Gold	Silica	Gold
α (°)	60° ± 1°	55° ± 1°	79° ± 2°	50° ± 1°
β (°)	144° ± 3°	96° ± 3°	112° ± 4°	107° ± 1°
γ (°)	145° ± 4°	149° ± 3°	124° ± 2°	114° ± 2°

[a] Averaged over the last 30 ns of MD.

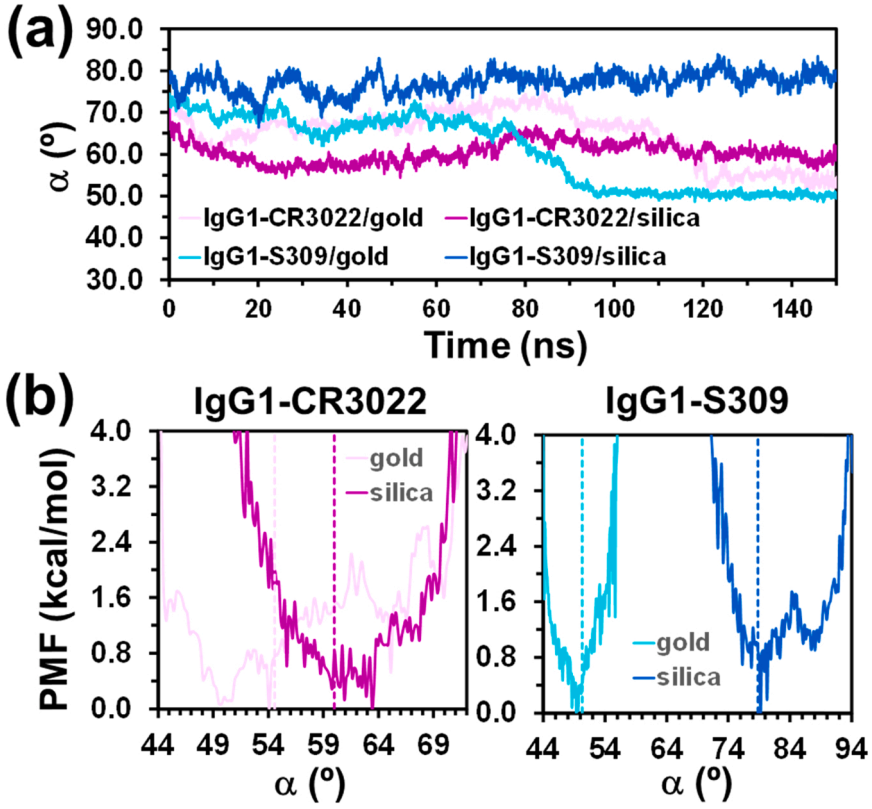

Fig. 2. (a) Temporal evolution of α along the cMD trajectories. (b) PMF profiles of α as derived from the aMD samplings for IgG1-CR3022 and IgG1-S309 tethered to the silica and gold surface. The dashed lines in the PMF profiles, which display the region with $\Delta G \leq 4.0$ kcal/mol, indicate the position of the average from cMD.

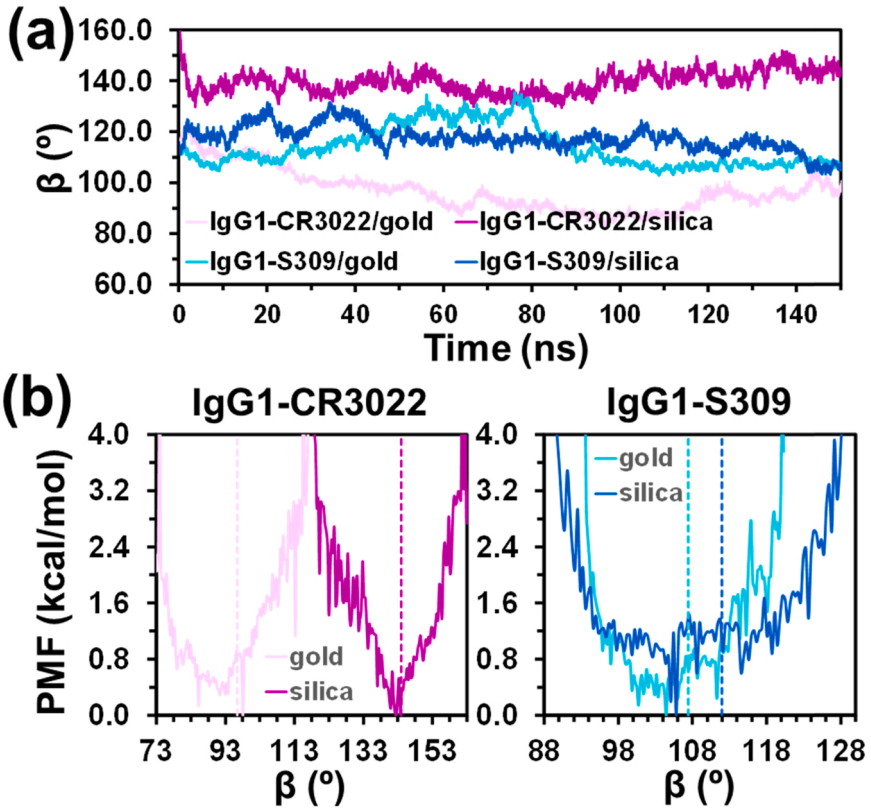

Fig. 3. (a) Temporal evolution of β along the cMD trajectories. (b) PMF profiles of β as derived from the aMD samplings for IgG1-CR3022 and IgG1-S309 tethered to the silica and gold surface. The dashed lines in the PMF profiles, which display the region with $\Delta G \leq 4.0$ kcal/mol, indicate the position of the average from cMD.

gold slabs, respectively, the TIP3P parameters for water [69], and the Li et al. parameters for solvated free ions [70]. The linker-silica and the linker gold bond distances, which were fixed at $d_{C\text{-}Si} = 1.86$ Å and $d_{C\text{-}Au} = 2.064$ Å, respectively, were estimated using density functional theory (DFT) calculations using small model systems. The RESP method [71] was used to obtain the point charges of the linkers.

2.4. Molecular dynamics protocol

All classical simulations were performed using the NAMD 2.13 simulation package [72]. AmberTools Leap program was used to set up input files for cMD and aMD simulations with NAMD. Surface atoms were considered frozen during the whole simulation process. Before starting the systems equilibration, they were minimized with all the protein atoms restrained to the crystal coordinates to remove close contacts, and the restrained system was gradually heated up to 298 K using an NVT ensemble along 50 ps. Covalent bonds involving hydrogen atoms were constrained using the SHAKE algorithm [73]. Long-range electrostatic interactions were treated with particle-mesh Ewald using a real-space cutoff of 10 Å [74]. The protein restraints were relaxed following the next 4 ns of simulations using a NPT ensemble at 1 atm and 298 K up to constant density. An integration time step of 2 fs was used in all MD simulations.

cMD simulations were extended for 150 ns using a NVT ensemble at 298 K with coordinates recorded every 40 ps. aMD was used to enhance the conformational sampling on the engineered antibodies by artificially reducing the energy barriers that separate different conformational states [75]. The parameters necessary to define the threshold of the potential energy and the extension of the modification applied to the potential profile were calculated from the averaged dihedral energy obtained at the end of 150 ns of cMD simulations (details are given in Supporting Information). aMD simulations were performed along 90 ns using an NVT ensemble and starting from 4 different snapshots for each engineered antibody, which were taken from cMD simulations. Accordingly, a total of 720 ns of aMD trajectories were produced.

3. Results and discussion

Firstly, to gain insight into the impact of the surfaces on the overall structure of the antibodies, we compared the root-mean-square deviation (RMSD), the root-mean-square fluctuations (RMSF) and the radius of gyration (R_g) of the two antibodies immobilized on silica and gold from the initial models. The four RMSD profiles, which were calculated considered all the backbone and side chains atoms, are shown in Fig. 1a. It is not surprising that there is a similar behavior for the two antibodies on each surface, indicating that those effects are associated with the surface chemistry govern the dynamics of the antibody while the sequence plays a crucial role on the final stability. The RMSD averaged during the last 70 ns of the trajectory, which are shown in Table 1, reflects that adsorbed IgG1-CR3022 is slightly more stable than IgG1-S309, independently of the surface properties. However, Fig. 1a shows a progressive and sustained increase of the RMSD until around 40 and 80 ns for the antibodies immobilized on silica and gold, respectively, independently of the sequence. This distinctive feature evidences that the influence of the surface properties on the kinetics of the structural rearrangement of the antibodies are higher for silica, which shows the highest rate.

The RMSF, which describes the amplitude of residue movement (fluctuation) from the average position (in the aligned structures) over the entire length of the cMD trajectories, is displayed in Fig. S3 for the four systems under study. As expected from RMSD analyses, residues from IgG1-CR3022 have generally fluctuated more than those from IgG1-S309, independently of the surface. Also, gold produces more homogeneous fluctuations than silica, even though the distortions caused by latter surface result not only in the regions with the highest fluctuations but also with the lowest ones. These observations are supported

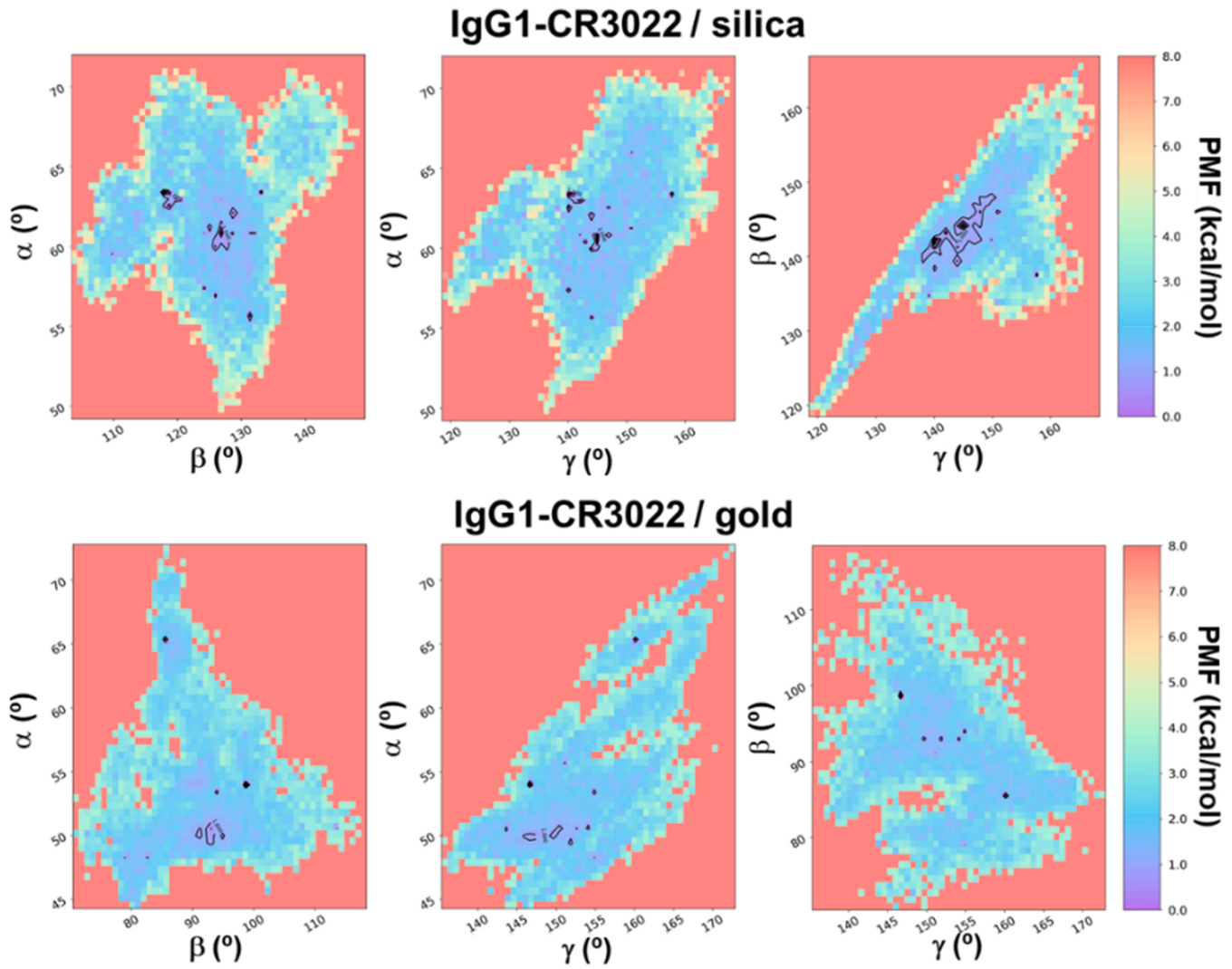

Fig. 4. *β–α* (left) *γ–α* (center) and *γ–β* (right) PMF maps from aMD samplings for IgG1-CR3022 tethered to silica (top) and gold (down). The positions of the minima are indicated in black.

by the average RMSF values, which are listed in Table 1. On the other hand, the effect of the different surfaces is compared in Fig. 1b, which represents the difference between the two RMSF values: ΔRMSF = RMSF(silica) – RMSF(gold). The surface chemistry had larger influence on IgG1-CR3022 than on IgG1-S309. Thus, the former antibody displayed a significant number of tracts with ΔRMSF > 5 Å, which were mainly located at the heavy chain (H in Scheme 1) of Fab1 (residues: 1–220) and at the light chain (L in Scheme 1) of Fab2 (residues: 891–1111), whereas ΔRMSF values tend to be significantly smaller for IgG1-S309.

The R_g of the four immobilized antibodies exhibited small fluctuations during the whole cMD trajectories, as is shown in Fig. 1c. However, the averages over the last 70 ns, which are included in Table 1, suggest that gold affected the mass distribution of IgG1-CR3022, causing a reduction of around 8% in the R_g. However, the R_g values individually calculated for the F_c, Fab1 and Fab2 fragments, which are plotted in Fig. S4, evidenced a similar behavior, independently of the engineered antibody and the surface. This feature indicated that the mass redistribution detected in Fig. 1c for IgG1-CR3022 tethered to gold was not due to local conformational changes but to the variation of the relative orientation between fragments. This point will be explicitly discussed below.

In order to ascertain the orientation of the immobilized antibodies with respect to the surface, the tilt (α) and the hinge (β and γ) angles were determined as shown in Scheme 3. More specifically, α was established as the angle formed by 1–2–3 where 1 is the silicon or gold atom, depending on the surface, 2 is the α-carbon atom of the Lys used to tether the antibody to the surface and situated at the bottom of the F_c region (*i.e.* Lys478 of IgG1-CR3022 and IgG1-S309), and 3 is the α-carbon atom of the Pro residue at the top of the F_c region (*i.e.* Pro245 for IgG1-CR3022 and the IgG1-S309, respectively). The hinge angles β and γ correspond to the angle between the Fc-Fab1 and Fc-Fab2 domains, respectively. These are defined by 2–3–4 and 2–3–5 in Scheme 3, respectively, where 4 and 5 are the center of mass of the complementary determining regions (CDR) in the Fab1 and Fab2 arms, respectively.

Fig. 2a shows the temporal evolution of α for the two antibodies immobilized on silica and gold. As it can be seen, the tilting was lower for antibodies tethered on the former surface than on the latter one, this feature being especially remarkable for IgG1-S309 (Table 2). Fig. 2b compares the potential of mean force (PMF) free energy profiles for α as determined from aMD simulations. For the sake of clarity, the two profiles obtained for each surface, silica and gold, are displayed together (IgG1-CR3022 and IgG1-S309 at left and right, respectively), the region with $\Delta G \leq 4.0$ kcal/mol being the only shown.

For IgG1-CR3022, the two profiles present significant differences (Fig. 2b, left). Thus, for the protein immobilized on gold, the region of the profile with $\Delta G \leq 4.0$ kcal/mol extends by almost 30° and exhibits several well-defined local minima very close in position and energy to

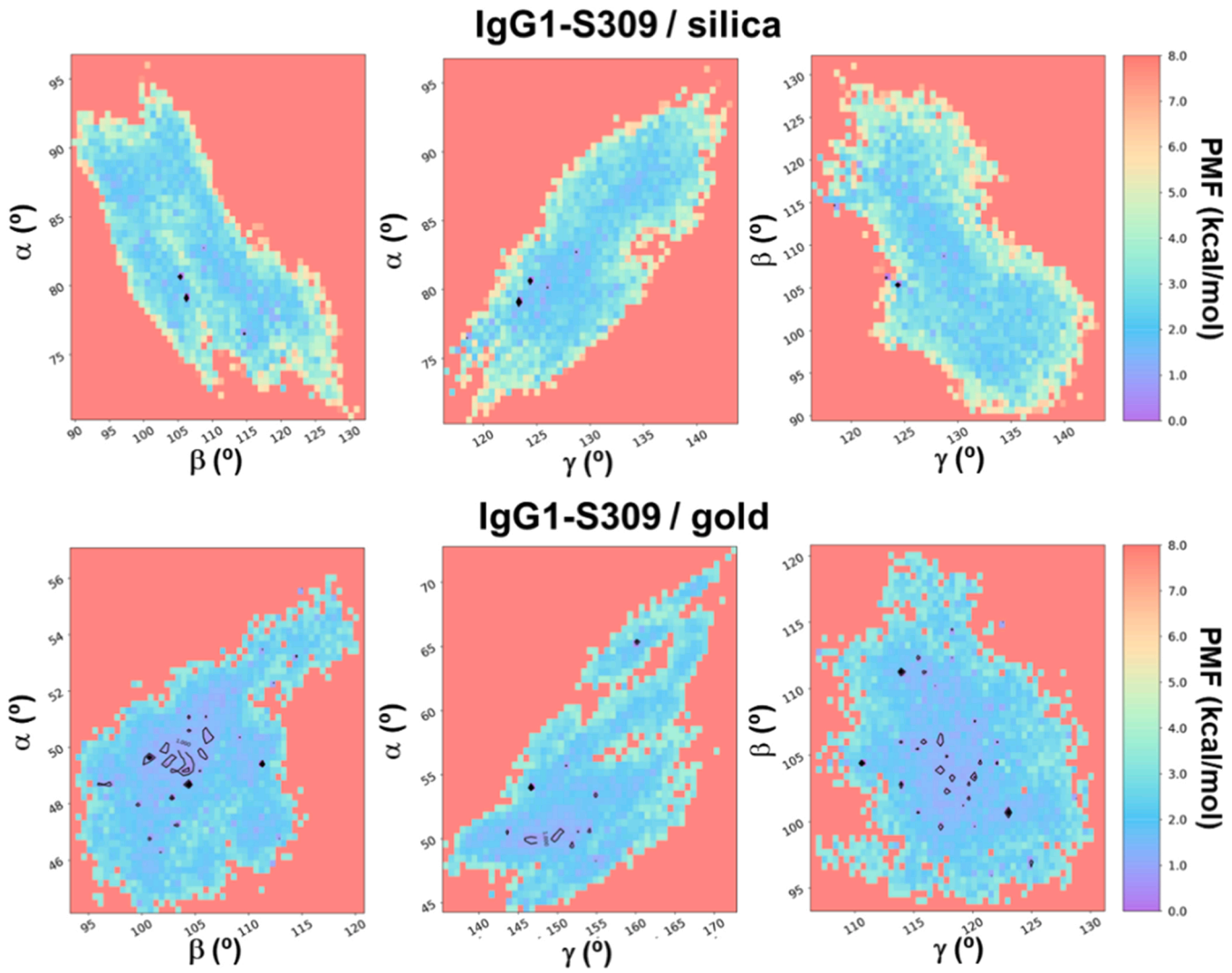

Fig. 5. β–α (left) γ–α (center) and γ–β (right) PMF maps from aMD samplings for IgG1-S309 tethered to silica (top) and gold (down). The positions of the minima are indicated in black.

the global minimum, α = 54º. Instead, the antibody immobilized on silica displays a much narrower profile with a well-defined global minimum at α = 63º. These results are fully consistent with those achieved by cMD, reflecting that in both cases the position of the global minima are very close to the average values derived from Fig. 2a. Furthermore, the latter value is in agreement with that obtained for pristine IgG1 B12 immobilized on silica (α = 66º) [76], indicating that the incorporation of the Fab of CR3022 in the engineered antibody does not affect to the orientation with respect to the substrate.

On the other hand, two narrow profiles with a well-defined global minimum were obtained for IgG1-S309 (Fig. 2b, right). However, the position of the global minimum, which corresponds to α = 79º and 49º for silica and gold, respectively, suggests that inclination of this protein with respect to the surface strongly depends on the protein–surface interactions. Thus, the balance between attractive and repulsive electrostatic interactions involving the charged surface atoms and the charged antibody residues probably avoids the tilt of IgG1-S309 over the silica substrate, whereas attractive short range van der Waals interactions is expected to favor the inclination of the antibody over the gold surface. As occurred for IgG1-CR3022, the global minimum found for IgG1-S309 on the two surfaces using aMD and cMD are in very good agreement.

Fig. 3 displays the temporal evolution of the hinge angle β for the four studied systems and the PMF profiles derived from aMD simulations. In this case, the IgG1-S309 antibody β was found to be practically independent of the surface chemistry (Fig. 3a and Table 2). Although the values listed in Table 2 are relatively close to that obtained for the crystal structure of IgG1 B12 antibody [51], which is 96º, the difference (16º and 11º, respectively) is large enough to reflect some influence of the isotropic forces exerted by the surfaces on the engineered antibody. Consistently, the PMF free energy profiles obtained for IgG1-S309 on silica and gold were very similar (Fig. 3b), having a well-defined global minimum at 106º and 104º, respectively. The influence of the surface was much higher for IgG1-CR3022, which exhibited an average value of 144º ± 3º and 96º ± 3º when immobilized on silica and gold, respectively (Fig. 3a). Besides, aMD simulations revealed two separated PMF profiles with a very well-defined minimum close the above mentioned values (*i.e.* 144º and 98º, respectively). Interestingly, in the case of IgG1-CR3022, the difference between the β value derived from simulations and the crystal structure of IgG1 B12 antibody was very small for gold and maximal for silica (2º and 48º, respectively).

Similar observations were attained for the hinge angle γ, as is evidenced in Fig. S5. In this case, the average values derived from cMD simulations depended more on the antibody than on the surface (Fig. S5a). For IgG1-CR2022, the γ value, averaged from the last 30 ns of simulation, which are included in Table 2, were larger than the average observed in the crystal structure of IgG1 B12 (123º) [52]. Besides, the averaged γ value decreased for IgG1-S309 immobilized on silica and gold (Table 2), which was consistent with the behavior displayed in

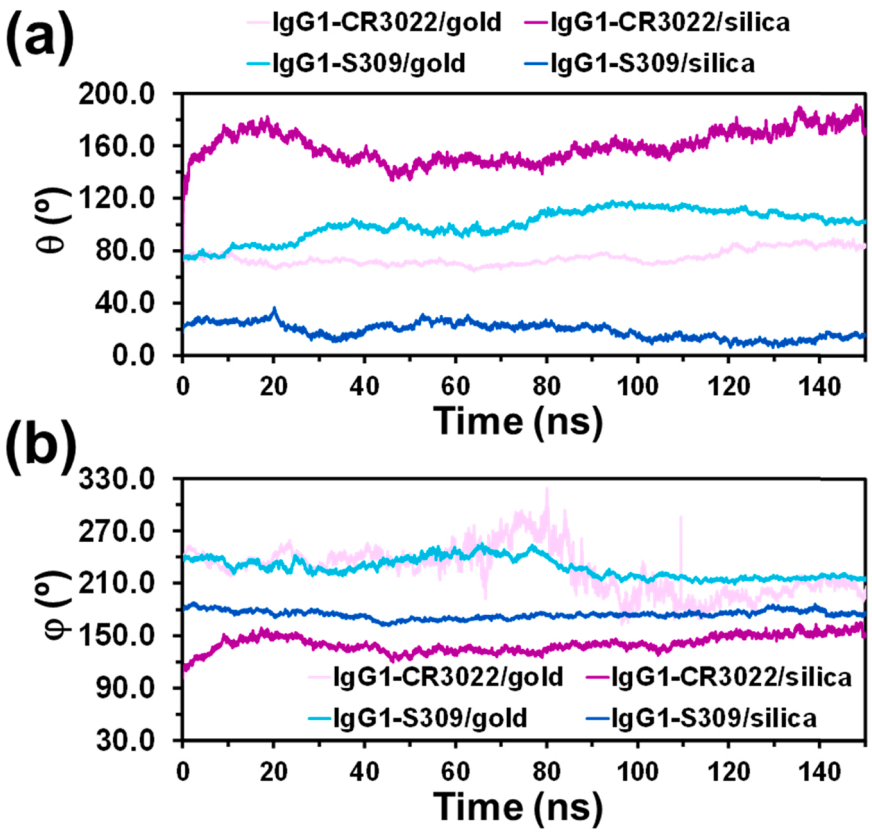

Fig. 6. Temporal evolution of (a) θ and (b) φ along the cMD trajectories.

Fig. 3 for β. Although the PFM profiles displayed in Fig. S5b are in agreement with such differences, the PMF profile calculated for IgG1-CR3022 tethered on silica exhibited an important difference with respect to the rest of the profiles. This is the presence of a local minimum at 127°, which is very close to the γ value in the crystal structure of IgG1 B12, that was destabilized with respect to the global minimum (144°) by 0.9 kcal/mol only. The other three profiles presented a single and well-defined minimum located at a value close to that derived from cMD, in fine agreement with results displayed in Figs. 2 and 3.

Analysis of {β,γ} pairs reveals that $\beta \approx \gamma$ for IgG1-CR3022 immobilized on silica ($\beta = 144° \pm 3°$, $\gamma = 145° \pm 4°$) and IgG1-S309 tethered to silica ($\beta = 112° \pm 4°$, $\gamma = 124° \pm 4°$) and gold ($\beta = 107° \pm 1°$, $\gamma = 114° \pm 4°$) with $\Delta = 1°$, 12° and 7°, respectively, where $\Delta = |\beta - \gamma|$. Conversely, Δ increases to 53° for IgG1-CR3022 immobilized on gold ($\beta = 96° \pm 3°$, $\gamma = 149° \pm 3°$). This behavior is fully consistent with the R_g values discussed above for the four studied systems (Fig. 1c). Those results showed that the R_g of IgG1-S309 tethered to gold exhibited a reduction of ~8% with respect to the value obtained for silica, whereas the similar R_g values were found for IgG1-S309 immobilized on gold and silica. Preliminary individual analyses of the F_c, Fab1 and Fab2 suggested that the reduction observed for IgG1-CR3022 on gold was probably due to differences in the orientation of the fragments, which has been confirmed by the high Δ value. These results indicate that Fab1···Fab2 repulsions predominate over Fab1···surface and Fab2···surface interactions when IgG1-CR3022 is on gold, while the opposite occurs when the protein is on silica. The fact that this difference is not observed for IgG1-S309 reflects that the sequence also plays an important role in the relative strength of the interactions and that, therefore, *in silico* studies require precise modeling techniques that include explicitly chemical details.

The influence of the surface of the relationships between of the tilt angle, α, and the hinge angles, β and γ, was investigated through the β–α, γ–α and γ–β PMF maps, which are displayed in Figs. 4 and 5 for IgG1-CR3022 and IgG1-S309, respectively. Comparison of the regions with lower free energies (≤ 1.5 kcal/mol) and the minima (indicated in black) obtained for IgG1-CR3022 on silica and gold (Fig. 4) reflects that the hinge angles do not show a clear relationship with α, independently of the surface. Thus, β–α and γ–α maps show that both the hinge and the tilt angles vary within relatively wide intervals. Conversely, analysis of the γ–β PMF maps indicates a very significant influence of the surface, even though both Fab1 and Fab2 arms exhibit pronounced flexibility for the two surfaces. However, the *β* and *γ* angles behave independently when the antibody is tethered to gold, while they are strongly correlated when the tethering is to silica. This feature, which is consistent with the PMF profiles previously discussed, has been attributed to the influence of the strength of the attractive interactions between the arms and the silica surface.

Inspection of the PMF maps calculated for IgG1-S309 on silica and gold (Fig. 5) reflected some similar features. Specifically, the tilt and hinge angles exhibited a wide range of values below a free energy threshold of 2 kcal/mol, suggesting that they tend to be independent. However, comparison of the γ–β PMF maps with those displayed in Fig. 4 evidences that the influence of the surface on the correlation between Fab1 and Fab2 arms is lower for IgG1-S309 than for obtained for IgG1-CR3022. Thus, the dependence between *β* and *γ* angles is practically inexistent when the IgG1-S09 is tethered to gold, and poor when the antibody is immobilized on silica.

On the other hand, comparison of the γ–β PMF maps obtained for IgG1-CR3022 and IgG1-S309 reveals some important differences in the correlation between the two hinge angles, especially when the antibodies are tethered to amorphous silica. This has been attributed to the effect of the interactions between the residues of the antibody and the polar atoms of the silica surface. More specifically, the primary structures of IgG1-CR3022 and IgG1-S309 differ in the Fab and Fv fragments (Scheme 1). Thus, the Fab fragment of IgG1-CR3022 and the Fv fragment of IgG1-S309 are significantly rich in polar and charged residues,

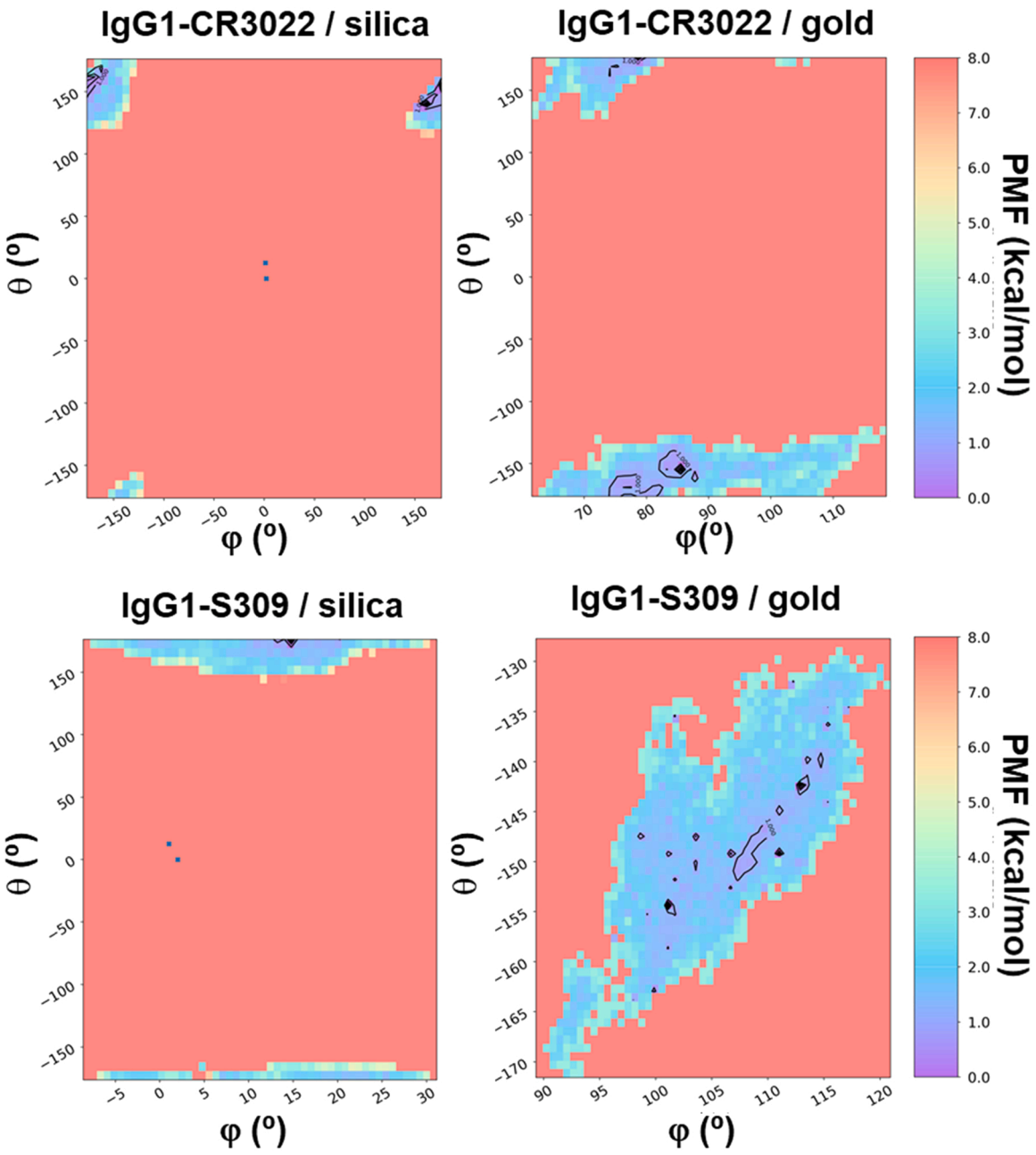

Fig. 7. θ–φ PMF maps from aMD samplings for IgG1-CR3022 (top) and IgG1-S309 (down) tethered to silica (left) and gold (right). The positions of the minima are indicated in black.

explaining their tight bound to the RBD of SARS-CoV-2 spike [36,37]. This structural difference affects the strength of the silica···antibody interactions, which in turn alter the preferences and correlation between the two hinge angles.

The temporal evolution of the angle defined by the Fab1 and Fab2, which is named δ and defined by 4–3–5 in Scheme 3, is displayed in Fig. S6. As it was expected, this angle was strongly influenced by the chemistry of the surface, exhibiting a similar behavior for two proteins immobilized on silica (*i.e.* averages over the last 30 ns: 119° ± 2° and 122° ± 3° for IgG1-CR3022 and IgG1-S309, respectively) and for the two proteins immobilized on gold (*i.e.* 99° ± 4° and 100° ± 4° for IgG1-CR3022 and IgG1-S309, respectively). Interestingly, the δ values obtained for the proteins on silica were ~20° greater than those on gold, confirming our previous assumption that Fab1···silica and Fab2···silica interactions are attractive and stronger than for gold.

The orientation of the antibodies anchored on the silica and gold surfaces was investigated by evaluating the dihedrals θ and φ, which are defined by 1–2–3–4 and 1–2–3–5 in Scheme 3, respectively. The temporal evolution of those parameters is represented in Fig. 6. As it was expected, the dihedrals, which remained relatively stable over the whole simulations, were strongly affected by the chemistry of the surfaces. The θ / φ values averaged over the last 50 ns of the simulations on IgG1-CR3022 and IgG1-S309 immobilized on gold were 86° ± 2° / − 157° ± 9° and 104° ± 3° / − 144° ± 2°, respectively. These values indicate that the influence of short range interactions between the antibodies and the inert gold atoms does not play any relevant role on the orientation of the protein. Indeed, the differences observed between the two antibodies, which are lower than 20°, were mainly attributed to the structural perturbations induced by the different sequences. Conversely, long-range electrostatic interactions involved the charged atoms of silica and ionized residues of the proteins drastically affected the orientation of the two antibodies. Thus, the averaged θ / φ values were 176° ± 6° /

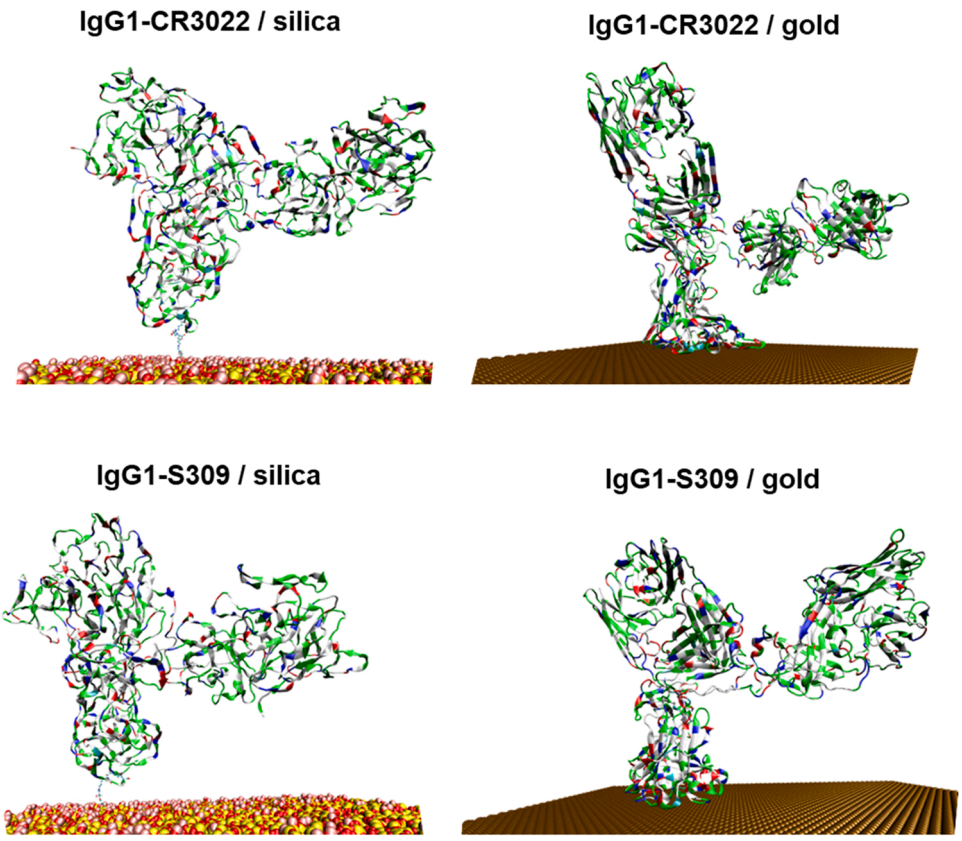

Fig. 8. Last snapshot recorded from cMD simulations for the four studied systems. Non-polar, polar, positively charged and negatively charges residues are displayed in grey, green, blue and red, respectively. (For interpretation of the references to colour in this figure, the reader is referred to the web version of this article.)

153º ± 4º and 12º ± 3º / 178º ± 3º for IgG1-CR3022 and IgG1-S309 immobilized on silica, respectively. These values differ significantly for the two antibodies and, in addition, are remarkably different from those obtained for gold, evidencing the drastic role of the substrate on the sensing process.

The effect of the surface-protein electrostatic interactions is reflected in Fig. S7, which displays for the four studied systems the variation of the total electrostatic energy as a function of the distance between the center of mass of the Fab arms (*i.e.* the average value for Fab1 and Fab2, hereafter named $d_{Fab\text{-}surface}$) and the surface. As it can be seen, the global minimum obtained for IgG1-CR3022 and IgG1-S309 immobilized on silica is larger that found for the same proteins on gold (17.3 and 4.4 Å, respectively). Although the total electrostatic energy is obviously influenced by the protein sequence, which drastically affects both protein-protein and protein-water interactions, the chemical nature of the surface also plays a key role. Thus, the silica-protein interactions are dominated by the charged atoms at the surface while gold-protein interactions only occur through van der Waals forces.

The dependence between θ and φ is displayed in Fig. 7, which shows the 2D PMF maps from aMD samplings for IgG1-CR3022 and IgG1-S309 tethered to silica and gold. As it can be seen, the topography of θ–φ depends not only on the substrate but also on the primary structure. Thus, for the two substrates, the maps are flatter for IgG1-S309 than for IgG1-CR3022, while for the two antibodies the maps are flatter for gold than for silica. This feature evidences that the biosensing process is affected by both the design of the antibody and the choice of the surface, which exhibit inter-dependence.

Finally, Fig. 8 compares the final structure derived from cMD for each studied system. As it can the seen, the interactions between the proteins and the silica surface results not only in a suitable orientation of the antibodies but also in a stabilization of the Y-shaped structure. Although these features are observed for both IgG1-CR2022 and IgG1-S309, they are more pronounced for the former than for the latter, as is evidenced by the partial fraying of the Fab1. On the other hand, the strength of the interactions between the Fab1···Fab2 arms seems to dominate over those between the protein and the gold surface. This fact results the fraying of both the Fab1 and Fab2 and, therefore, the fragmentary mislaying of the characteristic Y-shape structure in both antibodies.

Although the current classical force-fields used to model protein, including antibody, interactions were developed for aqueous environment, their combination with parameters optimized to model inorganic surfaces usually provides a good a qualitative description of protein-surface interactions. Undoubtedly, the main challenge in the simulation of antibody-surface systems is the sampling that, in some cases, is not possible using cMD simulations. In this work, this challenge has been overcome by complementing cMD with aMD, which ensures a much more complete sample of the phase space at a very reasonable computational cost. Although electronic effects, such as polarization, are usually neglected by conventional classical force-fields, their advantages in terms of sampling and computational efficiency clearly outweigh the possible loss of accuracy.

4. Conclusions

On concluding remarks, the efficiency of immunosensors largely depends on the orientation and stability of the immobilized antibodies. However, there is a limited microscopic understanding of the influence of surface-proteins systems for achieving suitable appropriate orientation when specific antibodies are analyzed. In this work, the orientation of two antibodies, IgG1-CR3022 and IgG-S309, which were specifically designed to detect SARS-CoV-2 spike, immobilized on amorphous silica and gold has been analyzed and compared *in silico* using MD simulations. The differences in atomic fluctuations of each antibody when comparing

the immobilized protein on both surfaces showed a greater surface chemistry influence in IgG1-CR3022 than in the IgG1-S309 system. The amorphous silica substrate offers a more appropriate orientation and has less impact on the Y-shape structure of antibodies than gold. Indeed, the tilt angle (α) of IgG1-CR3022 immobilized on silica is very close to that obtained for pristine IgG1 B12 immobilized on silica ($\Delta\alpha = -3^{o}$) and in less extend to IgG1-S309 ($\Delta\alpha = 12^{o}$), indicating that the incorporation of the fragment antigen binding (Fab) of CR3022 in the engineered antibody is much less affected to the orientation with respect to the substrate when is compared with the incorporation of just the variable fragment (Fv) of S309. This has been attributed to the surface chemistry of amorphous silica, which contains polar and charged atoms, able to stablish long-range interactions with the protein. Conversely, the short-range van der Waals interactions between the gold surface and the protein favor a higher distortion in terms of orientation. Also, our results show that the role of surface chemistry on the orientation and stability predominates over the antibody primary structure.

In summary, *in silico* studies provide very reliable information for the design and development of immunosensors. Among the four systems studied in this work, IgG1-CR3022 immobilized on amorphous silica is the most promising for the detection of SARS-CoV-2 spike.

CRediT authorship contribution statement

Didac Martí: Investigation, Formal analysis, Writing – review & editing. **Eduard Martí-Martinez:** Investigation, Formal analysis, Writing – review & editing. **Juan Torras:** Funding acquisition, Supervision, Validation, Formal analysis, Methodology, Writing – review & editing. **Oscar Bertran:** Validation; Writing – review & editing. **Pau Turon:** Funding acquisition, Supervision, Formal analysis, Writing – review & editing. **Carlos Alemán:** Funding acquisition, Supervision, Formal analysis, Writing – original draft, Writing – review & editing.

Declaration of Competing Interest

The authors declare that they have no known competing financial interests or personal relationships that could have appeared to influence the work reported in this paper.

Acknowledgements

J.T. acknowledges “Partnership for Advanced Computing in Europe” (PRACE) for awarding us access to Joliot-Curie at GENCI@CEA(Irene), France, through the “PRACE support to mitigate impact of COVID-19 pandemic” call. CA Acknowledges the Agència de Gestió d′Ajuts Universitaris i de Recerca (2017SGR359) and B. Braun Surgical, S.A.U. for financial support.

Appendix A. Supporting information

Supplementary data associated with this article can be found in the online version at doi:10.1016/j.colsurfb.2022.112400.

References

[1] A.D. Radadia, C.J. Stavis, R. Carr, H. Zeng, W.P. King, J.A. Carlisle, A. Aksimentiev, R.J. Hamers, R. Bashir, Control of nanoscale environment to improve stability of immobilized proteins on diamond surfaces, Adv. Funct. Mater. 21 (2011) 1040–1050.
[2] Y. Dong, X. Ji, A. Laaksonen, W. Cao, H. He, X. Lu, Excellent protein immobilization and stability on heterogeneous C–TiO_2 hybrid nanostructures: a single protein AFM study, Langmuir 36 (2020) 9323–9332.
[3] M. Hoarau, S. Badieyan, E.N. Marsh, Immobilized enzymes: Understanding enzyme–surface interactions at the molecular level, Org. Biomol. Chem. 15 (2017) 9539–9551.
[4] G.A. Somorjai, Y. Li, Impact of surface chemistry, Proc. Nat. Acad. Sci. USA 108 (2011) 917–924.
[5] C. Coscolín, A. Beloqui, M. Martínez-Martínez, R. Bargiela, G. Santiago, R. M. Blanco, G. Delaittre, C. Márquez-Álvarez, M. Ferrer, Controlled manipulation of enzyme specificity through immobilization-induced flexibility constraints, Appl. Catal. A 565 (2018) 59–67.
[6] T. Montes, V. Grazu, F. López-Gallego, J.A. Hermoso, J.M. Guisan, R. Fernandez-Lafuente, Chemical modification of protein surfaces to improve their reversible enzyme immobilization on ionic exchangers, Biomacromolecules 7 (2006) 3052–3058.
[7] R.A. Latour, Fundamental principles of the thermodynamics and kinetics of protein adsorption to material surfaces, Colloids Surf. B 191 (2020), 110992.
[8] M. Ozboyaci, D. Kokh, S. Corni, R. Wade, Modeling and simulation of protein–surface interactions: achievements and challenges, Q. Rev. Biophys. 49 (2016), E4.
[9] B. Jachimska, S. Swiatek, J.I. Loch, K. Lewinski, T. Luxbacher, Adsorption effectiveness of β-lactoglobulin onto gold surface determined by quartz crystal microbalance, Bioelectrochemistry 121 (2018) 95–104.
[10] H. Noguchi, T. Adachi, A. Nakatomi, M. Yazawa, K. Uosaki, Biofunctionality of calmodulin immobilized on gold surface studied by surface-enhanced infrared absorption spectroscopy: Ca^{2+}-Induced conformational change and binding to a target peptide, J. Phys. Chem. C. 120 (2016) 16035–16041.
[11] X. Wu, K. Fraser, J.S. Dordick, X. Wu, K. Fraser, J. Zha, J.S. Dordick, Flexible peptide linkers enhance the antimicrobial activity of surface-immobilized bacteriolytic enzymes, ACS Appl. Mater. Interfaces 10 (2018) 36746–36756.
[12] R. Cademartiri, H. Anany, M.A. Brook, Immobilization of bacteriophages on modified silica particles, Biomaterials 31 (2010) 1904–1910.
[13] M. Ray, S.D. Mhaske, S. Mazumdar, M. Ray, S.D. Mhaske, S.K. Haram, S. Mazumdar, Covalent conjugation of single-walled carbon nanotube with CYP101 mutant for direct electrocatalysis, Anal. Biochem. 626 (2021), 114204.
[14] M. Murphy, K. Theyagarajan, K. Thenmozhi, S. Senthilkumar, T.K. Theyagarajan, Direct electrochemistry of covalently immobilized hemoglobin on a naphthylimidazolium butyric acid ionic liquid/MWCNT matrix, Colloids Surf. B 199 (2021), 111540.
[15] E.D. Sitsanidis, J. Schirmer, M. Pettersson, E.D. Sitsanidis, J. Schirmer, A. Lampinen, K.K. Mentel, V.-M. Hiltunen, V. Ruokolainen, A. Johansson, P. Myllyperkiö, M. Nissinen, M. Pettersson, Tuning protein adsorption on graphene surfaces via laser-induced oxidation, Nanoscale Adv. 3 (2021) 2065–2074.
[16] W.Q. Lai, B.C. Lin, Z.G. Xi, L. Wenqing, L. Bencheng, Z. Wei, Y. Jun, L. Huanliang, X. Zhuge, The amino-functionalized graphene oxide nanosheet preparation for enzyme covalent immobilization, J. Nanosci. Nanotechnol. 20 (2020) 7398–7405.
[17] X.Q. Pang, W.Q. Li, H.S. Azevedo, X. Pang, W. Li, L. Chang, G. Lan, J.E. Gautrot, W. Wang, H.S. Azevedo, Hyaluronan (HA) immobilized on surfaces via self-assembled monolayers of ha-binding peptide modulates endothelial cell spreading and migration through focal adhesion, ACS Appl. Mater. Interfaces 13 (2021) 25792–25804.
[18] S.J. Yang, J. Liu, J. Zhou, S. Yang, J. Liu, H. Zheng, J. Zhong, J. Zhou, Simulated revelation of the adsorption behaviours of acetylcholinesterase on charged self-assembled monolayers, Nanoscale 12 (2020) 3701–3714.
[19] Y. Dong, X. Ji, A. Laaksonen, W. Cao, R. An, L. Lu, X. Lu, Determination of the small amount of proteins interacting with TiO_2 nanotubes by AFM-measurement, Biomaterials 192 (2019) 368–376.
[20] Y. Dong, R. An, S. Zhao, W. Cao, L. Huang, W. Zhuang, L. Lu, X. Lu, Molecular interactions of protein with TiO_2 by the AFM-measured adhesion force, Langmuir 33 (2017) 11626–11634.
[21] A. Fahs, G. Louarn, Plant protein interactions studied using AFM force spectroscopy: nanomechanical and adhesion properties, Phys. Chem. Chem. Phys. 15 (2013) 11339–11348.
[22] Y. Yamamoto, H. Kominami, K. Kobayashi, H. Yamada, Surface charge density measurement of a single protein molecule with a controlled orientation by AFM, Biophys. J. 120 (2021) 2490–2497.
[23] Z.C. Lou, B. Wang, Z. Lou, B. Wang, C. Guo, K. Wang, H. Zhang, B. Xu, Molecular-level insights of early-stage prion protein aggregation on mica and gold surface determined by AFM imaging and molecular simulation, Colloids Surf. B 135 (2015) 371–378.
[24] J.M. Bolivar, B. Nidetzky, On the relationship between structure and catalytic effectiveness in solid surface-immobilized enzymes: Advances in methodology and the quest for a single-molecule perspective, Biochim. Biophys. Acta Proteins Proteom. 1868 140333 (2020).
[25] D. Martí, E. Martín-Martínez, J. Torras, O. Bertran, P. Turon, C. Alemán, *In silico* antibody engineering for SARS-CoV-2 detection, Comput. Struct. Biotechnol. J. 19 (2021) 5525–5534.
[26] D.F. Marruecos, D.K. Schwartz, J.L. Kaar, Impact of surface interactions on protein conformation, Curr. Opin. Colloid Interface Sci. 38 (2018) 45–55.
[27] R.F. Sabirianov, A. Rubinstein, F. Namavar, Enhanced initial protein adsorption on engineered nanostructured cubic zirconia, Phys. Chem. Chem. Phys. 13 (2011) 6597–6609.
[28] X. Zou, S. Wei, S. Badieyan, M. Schroeder, J. Jasensky, C.L. Brooks 3rd, E.N. G. Marsh, Z. Chen, Investigating the effect of two-point surface attachment on enzyme stability and activity, J. Am. Chem. Soc. 5 (2018) 16560–16569.
[29] O. Bertran, D. Curcó, D. Zanuy, C. Alemán, Atomistic organization and characterization of tube-like assemblies comprising peptide–polymer conjugates: computer simulation studies, Faraday Discuss. 166 (2013) 59–82.
[30] A. Kumar, D. Ghosh, M. Radhakrishna, Surface patterning for enhanced protein stability: insights from molecular simulations, J. Phys. Chem. B 123 (2019) 8363–8369.
[31] D.C. Malaspina, L. Perez-Fuentes, C. Drummond, D. Bastos-Gonzalez, J. Faraudo, Protein-surface interactions at the nanoscale: Atomistic simulations with implicit solvent models, Curr. Opin. Colloid Interface Sci. 41 (2019) 40–49.

[32] G. Brancolini, V. Tozzini, Multiscale modeling of proteins interaction with functionalized nanoparticles, Curr. Opin. Colloid Interface Sci. 41 (2019) 66–73.
[33] X.B. Quan, J. Liu, J. Zhou, Multiscale modeling and simulations of protein adsorption: progresses and perspectives, Curr. Opin. Colloid Interface Sci. 41 (2019) 74–85.
[34] Y. Ma, S. Velioğlu, T.A. Trinh, R. Wang, J.W. Chew, Investigation of surfactant–membrane interaction using molecular dynamics simulation with umbrella sampling, ACS EST Engg 1 (2021) 1470–1480.
[35] S. Lecot, Y. Chevolot, M. Phaner-Goutorbe, C. Yeromonahos, Impact of silane monolayers on the adsorption of streptavidin on silica and its subsequent interactions with biotin: molecular dynamics and steered molecular dynamics simulations, J. Phys. Chem. B 124 (2020) 6786–6796.
[36] F. Krammer, SARS-CoV-2 vaccines in development, Nature 586 (2020) 516–527.
[37] C.B. Creech, S.C. Walker, R.J. Samuels, SARS-CoV-2 vaccines, JAMA 325 (2021) 1318–1320.
[38] G. Kampf, D. Todt, S. Pfaender, E. Steinmann, Persistence of coronaviruses on inanimate surfaces and their inactivation with biocidal agents, J. Hosp. Infect. 104 (2020) 246–251.
[39] M.L. Smith, S. Gandolfi, P.M. Coshall, P.K.S.M. Rahman, Biosurfactants: A Covid-19 perspective, Front. Microbiol. 11 (2020) 1341.
[40] A.S. Jureka, J.-A. Silvas, C.F. Basler, Propagation, inactivation, and safety testing of SARS-CoV-2, Viruses 12 (2020) 622.
[41] J.P. Abraham, B.D. Plourde, L. Cheng, Using heat to kill SARS-CoV-2, Rev. Med. Virol. 30 (2020), e2115.
[42] D. Martí, J. Torras, O. Bertran, P. Turon, C. Alemán, Temperature effect on the SARS-CoV-2: A molecular dynamics study of the spike homotrimeric glycoprotein, Comput. Struct. Biotechnol. J. 19 (2021) 1848–1862.
[43] A. Filipić, I. Gutierrez-Aguirre, G. Primc, M. Mozetič, D. Dobnik, Cold plasma, a new hope in the field of virus inactivation, Trends Biotechnol. 38 (2020) 1278–1291.
[44] M. Buonanno, D. Welch, I. Shuryak, D.J. Brenner, Far-UVC light (222 nm) efficiently and safely inactivates airborne human coronaviruses, Sci. Rep. 10 (2020) 10285.
[45] J. Li, Rui Lin, Y. Yang, R. Zhao, S. Song, Y. Zhou, J. Shi, L. Wang, H. Song, R. Hao, Multichannel immunosensor platform for the rapid detection of SARS-CoV-2 and Influenza A(H1N1) virus, ACS Appl. Mater. Interfaces 13 (2021) *22262*–22270.
[46] L.F. de Lima, A.L. Ferreira, M.D.T. Torres, W.R. de Araujo, C. de la Fuente-Nuñez, Minute-scale detection of SARS-CoV-2 using a low-cost biosensor composed of pencil graphite electrodes, Proc. Natl. Acad. Sci. USA 118 (2021), e2106724118.
[47] I.A. Mattioli, A. Hassan, O.N. Oliveira, F.N. Crespilho, On the challenges for the diagnosis of SARS-CoV-2 based on a review of current methodologies, ACS Sens. 5 (2020) 3655–3677.
[48] L. Huang, L. Ding, J. Zhou, S. Chen, F. Chen, C. Zhao, J. Xu, W. Hu, J. Ji, H. Xu, G. L. Liu, One-step rapid quantification of SARS-CoV-2 virus particles via low-cost nanoplasmonic sensors in generic microplate reader and point-of-care device, Biosens. Bioelectron. 171 (2021), 112685.
[49] J. Huo, Y. Zhao, J. Ren, E.E. Fry, R.J. Owens, D.I. Stuart, Neutralization of SARS-CoV-2 by destruction of the prefusion spike, Cell Host Microbe 28 (2020) 445–454.
[50] D. Pinto, Y.J. Park, M. Beltramello, A.C. Walls, A. Tortorici, S. Bianchi, S. Jaconi, K. Culap, F. Zatta, A. De Marco, A. Peter, B. Guarino, R. Spreafico, E. Cameroni, J. B. Case, R.E. Chen, C.H. Daughton, G. Snell, A. Talenti, H.W. Virgin, A. Lanzavecchia, M.S. Diamond, K. Fink, D. Veesler, D. Corti, Cross-neutralization of SARS-CoV-2 by a human monoclonal SARS-CoV antibody, Nature 583 (2020) 290–295.
[51] E.O. Saphire, P.W. Parren, R. Pantophlet, M.B. Zwick, G.M. Morris, P.M. Rudd, R. A. Dwek, R.L. Stanfield, D.R. Burton, I.A. Wilson, Crystal structure of a neutralizing human IGG against HIV-1: A template for vaccine design, Science 293 (2001) 1155–1159.
[52] L. Du, Y. He, Y. Zhou, S. Liu, B.-J. Zheng, S. Jiang, The spike protein of SARS-CoV – a target for vaccine and therapeutic development, Nat. Rev. Microbiol. 7 (2009) 226–236.
[53] L. Du, Y. Yang, Y. Zhou, L. Lu, F. Li, S. Jiang, MERS-CoV spike protein: a key target for antivirals, Expert Opin. Ther. Targets 21 (2017) 131–143.
[54] X. Chi, X. Liu, C. Wang, Z. Chang, X. Li, J. Hou, L. Ren, Q. Jin, J. Wang, W. Yang, Humanized single domain antibodies neutralize SARS-CoV-2 by targeting the spike receptor binding domain, Natur. Commun. 11 (2020) 4528.
[55] D. Pinto, Y.-J. Park, M. Beltramello, A.C. Walls, M.A. Tortorici, S. Bianchi, S. Jaconi, K. Culap, F. Zatta, A. De Marco, A. Peter, B. Guarino, R. Spreafico, E. Cameroni, J.B. Case, R.E. Chen, C. Havenar-Daughton, G. Snell, A. Telenti, H. W. Virgin, A. Lanzavecchia, M.S. Diamond, K. Fink, D. Veesler, D. Corti, Cross-neutralization of SARS-CoV-2 by a human monoclonal SARS-CoV antibody, Nature 583 (2020) 290–295.
[56] M. Gierada, F. De Proft, M. Sulpizi, F. Tielens, Understanding the acidic properties of the amorphous hydroxylated silica surface, J. Phys. Chem. C 123 (2019) 17343–17352.
[57] D. Lin, T. Tang, D. Jed Harrison, W.E. Lee, A.B. Jemere, A regenerating ultrasensitive electrochemical impedance immunosensor for the detection of adenovirus, Biosens. Bioelectron. 68 (2015) 129–134.
[58] L.A.A. Chunduri, A. Kurdekar, M.K. Haleyurgirisetty, E.P. Bulagonda, V. Kamisetti, I.K. Hewlett, Femtogram level sensitivity achieved by surface engineered silica nanoparticles in the early detection of HIV infection, Sci. Rep. 7 (2017) 7149.
[59] V. Gubala, G. Giovannini, F. Kunc, M.P. Monopoli, C.J. Moore, Dye-doped silica nanoparticles: synthesis, surface chemistry and bioapplications, Cancer Nano 11 (2020) 1.
[60] A. Layqah, S. Eissa, An electrochemical immunosensor for the corona virus associated with the Middle East respiratory syndrome using an array of gold nanoparticle-modified carbon electrodes, Microchim. Acta 186 (2019) 224.
[61] H. Haji-Hashemi, P. Norouzi, M.R. Safarnejad, M.R. Ganjali, Label-free electrochemical immunosensor for direct detection of Citrus tristeza virus using modified gold electrode, Sens. Actuators B 244 (2017) 211–216.
[62] I.T. Todorov, W. Smith, K. Trachenko, M.T. Dove, DL_POLY_3: new dimensions in molecular dynamics simulations via massive parallelism, J. Mater. Chem. 16 (2006) 1911–1918.
[63] S. Munetoh, T. Motooka, K. Moriguchi, A. Shintani, Interatomic potential for si–o systems using tersoff parameterization, Comp. Mater. Sci. 39 (2007) 334–339.
[64] N.T. Huff, E. Demiralp, T. Çagin, W.A. Goddard III, Factors affecting molecular dynamics simulated vitreous silica structures, J. Non-Cryst. Solids 253 (1999) 133–142.
[65] D.A. Case, I.Y. Ben-Shalom, S.R. Brozell, D.S. Cerutti, T.E. Cheatham-III, V.W. D. Cruzeiro, T.A. Darden, R.E. Duke, D. Ghoreishi, M.K. Gilson, H. Gohlke, A. W. Goetz, D. Greene, R. Harris, N. Homeyer, Y. Huang, S. Izadi, S. Kovalenko, T. Kurtzman, T.S. Lee, S. LeGrand, P. Li, C. Lin, J. Liu, T. Luchko, R. Luo, D. J. Mermelstein, K.M. Merz, Y. Miao, G. Monard, C. Nguyen, H. Nguyen, I. Omelyan, A. Onufriev, F. Pan, R. Qi, D.R. Roe, A. Roitberg, C. Sagui, S. Schott-Verdugo, J. Shen, C.L. Simmerling, J. Smith, R. Salomon-Ferrer, J. Swails, R.C. Walker, J. Wang, H. Wei, R.M. Wolf, X. Wu, L. Xiao, D.M. York, P.A. Kollman, AMBER 2018, University of California, San Francisco, 2018.
[66] J.A. Maier, C. Martinez, K. Kasavajhala, L. Wickstrom, K.E. Hauser, C. Simmerling, ff14SB: improving the accuracy of protein side chain and backbone parameters from ff99SB, J. Chem. Theory Comput. 11 (2015) 3696–3713.
[67] N.T. Huff, E. Demiralp, T. Çagin, W.A. Goddard, Factors affecting molecular dynamics simulated vitreous silica structures, J. Non Cryst. Solids 253 (1999) 133–142.
[68] H. Heinz, R.A. Vaia, B.L. Farmer, R.R. Naik, Accurate simulation of surfaces and interfaces of face-centered cubic metals using 12-6 and 9−6 Lennard-Jones potentials, J. Phys. Chem. C 112 (2008) 17281–17290.
[69] W.L. Jorgensen, J. Chandrasekhar, J.D. Madura, R.W. Impey, M.L. Klein, Comparison of simple potential functions for simulating liquid water, J. Chem. Phys. 79 (1983) 926–935.
[70] P. Li, L.F. Song, K.M. Merz, Systematic parameterization of monovalent ions employing the nonbonded model, J. Chem. Theory Comput. 11 (2015) 1645–1657.
[71] C.I. Bayly, P. Cieplak, W.D. Cornell, P.A. Kollman, A well-behaved electrostatic potential based method using charge restraints for deriving atomic charges - the Resp model, J. Phys. Chem. 97 (1993) 10269–10280.
[72] J.C. Phillips, D.J. Hardy, J.D.C. Maia, J.E. Stone, J.V. Ribeiro, R.C. Bernardi, R. Buch, G. Fiorin, J. Hénin, W. Jiang, R. McGreevy, M.C.R. Melo, B.K. Radak, R. D. Skeel, A. Singharoy, Y. Wang, B. Roux, A. Aksimentiev, Z. Luthey-Schulten, L. V. Kalé, K. Schulten, C. Chipot, E. Tajkhorshid, Scalable molecular dynamics on CPU and GPU architectures with NAMD, J. Chem. Phys. 153 (2020), 044130.
[73] S. Miyamoto, P.A. Kollman, Settle: An analytical version of the SHAKE and RATTLE algorithm for rigid water models, J. Comput. Chem. 13 (1992) 952–962.
[74] C. Sagui, L.G. Pedersen, T.A. Darden, Towards an accurate representation of electrostatics in classical force fields: efficient implementation of multipolar interactions in biomolecular simulations, J. Chem. Phys. 120 (2004) 73.
[75] D. Hamelberg, J. Mongan, J.A. McCammon, Accelerated molecular dynamics: a promising and efficient simulation method for biomolecules, J. Chem. Phys. 120 (2004) 11919.
[76] D. Martí, J. Ainsley, O. Ahumada, C. Alemán, J. Torras, Tethering of the IgG1 antibody to amorphous silica for immunosensor development: a molecular dynamics study, Langmuir 36 (2020) 12658–12667.